Nonlinear Dynamics of Lateral Electrostatic Gap Closing Actuators for Applications in Inchworm Motors

Ahad M. Rauf, *Graduate Student Member, IEEE*, Daniel S. Contreras, Ryan M. Shih, Craig B. Schindler, and Kristofer S. J. Pister

Abstract—We present a nonlinear dynamics model for lateral electrostatic gap closing actuators (GCAs) operated in air and underwater. We factor in finger bending and the release phase's initial velocity over prior work, and we systematically study the effect on GCA pull-in and release time by varying both the finger length and the release spring constant. Simulation results are then compared to experimental data with good conformity. We also apply this dynamics model to optimize electrostatic inchworm motors for drive frequencies up to 40 kHz and speeds up to 415 mm/s, over 11× faster than what has been previously reported. **[2021-0197]**

Index Terms—Gap closing actuators, electrostatic inchworm motors, MEMS, dynamics.

Fig. 1. The unit cell of an unactuated GCA array. Dimensions of the fingers and spine used in the model are labeled.

I. INTRODUCTION

LATERALLY ORIENTED electrostatic gap closing actuators (GCAs) are useful for their low power draw and high areal force density. Since maximizing force output correlates with shrinking the size of the gap, these actuators are limited in the amount of displacement they can achieve, but this can be overcome by placing multiple actuators in an inchworm motor configuration [1]–[3]. Combining millimeter-scale displacements, force densities on the order of 1 mN/mm^2, and low power draw, these motors serve an important function in the microrobotics application space [4], [5].

The force output of GCA array-based inchworm motors has been well characterized in prior literature with excellent experimental verification [1]–[3]. However, forming an accurate model for these actuators' dynamics remains a challenging problem. Existing analyses of lateral electrostatic GCA dynamics tend to assume the capacitive fingers don't bend to ignore the effects of local deformations [6], [7] or only simulate resonance instead of the discrete phases of traditional inchworm actuation [8], [9]. A GCA's speed should relate
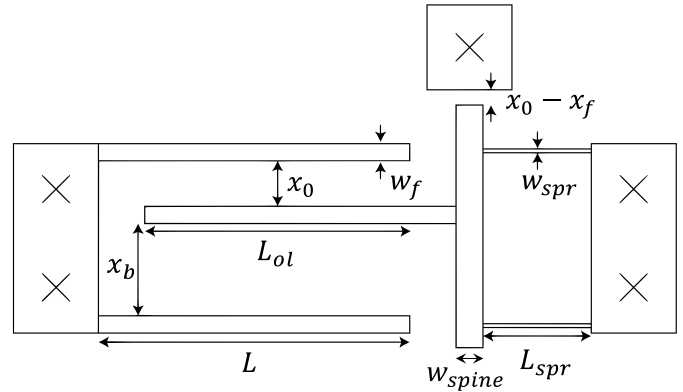
linearly to an inchworm motor's shuttle speed, and understanding the nonlinear dynamics behind GCAs can enable future optimization. By achieving faster shuttle speeds, these motors could drive microrobot legs to rival the speeds of insects.

This paper expands on previously presented work on the dynamics of GCA pull-in in air [10] and aqueous solutions [11]. We develop a model for the dynamics of GCA release over prior work, derive an equation for GCA finger bending, and compare our improved model to experimental data. We also expand our investigation on device performance to optimize an electrostatic inchworm motor for driving frequencies of up to 40 kHz and linear speeds of up to 415 mm/s.

II. THEORY

A. Dynamics of an Electrically Actuated Gap Closer Array

Fig. 1 shows the dimensions of the GCA fingers and central spine. Fingers have a length L, width w_f, and out-of-plane thickness T. The overlap length between fingers is given by L_{ol}. Before actuation, x_0 and x_b are the sizes of the front and rear gaps, respectively, between consecutive pairs of fingers. A central spine connects a total of N fingers together, and there are typically tens to hundreds of fingers per GCA. A gap stop in front of the spine maintains a final finger separation of x_f.

The equation of motion for an electrostatic GCA is

$$m_{GCA}\ddot{x} + b(x)\dot{x} + kx = F_{es}(x) \qquad (1)$$

where x is the lateral displacement of the movable finger array from its nominal position, m_{GCA} is the mass of the movable finger array, $b(x)$ is the damping coefficient, k is the spring
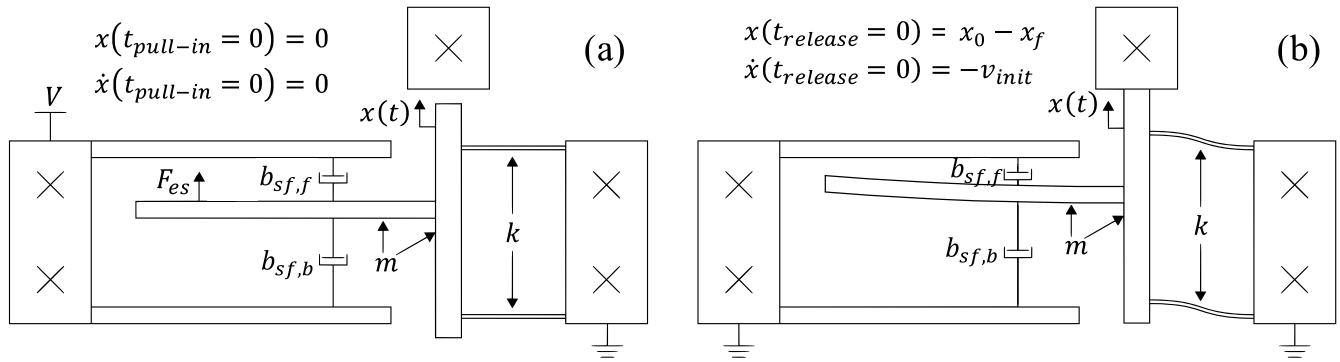
Fig. 2. A unit cell of the GCA array, highlighting the components of the dynamics equation. (a) The initial state of the system before pull-in. (b) The initial state of the system before release. The initial velocity is nonzero because of stored potential energy in the deformed fingers and spine. Our model assumes only the spine's fingers bend, explained further in the Appendix.

constant of the support spring, and $F_{es}(x)$ is the electrostatic actuation force. Once the finger array is pulled in, the central spine contacts the gap stop.

Release of the fingers is unactuated ($F_{es} = 0$) and relies on two support springs to reset the fingers' position. The initial velocity upon release is nonzero due to stored potential energy.

B. Gap Closer Dynamics in Air

Fig. 2 shows a unit cell of the GCA array during pull-in and release, highlighting the components of the dynamics equation.

The mass m_{GCA} in Eq. 1 comprises the full GCA array, including the central spine and support springs. This mass is

$$m_{GCA} = \rho_{Si} T A_{eff} \tag{2}$$

where ρ_{Si} is the density of silicon, T is the device silicon thickness, and A_{eff} is the area of the movable finger array after accounting for the lateral etch of the silicon during the DRIE step. This undercut significantly reduces the mass. Unfortunately, undercut tends to be highly process dependent and can vary from run to run. For our process, it varies between $0.2\,\mu\text{m} - 0.5\,\mu\text{m}$, averaging around $0.4\,\mu\text{m}$ [4], [11], [12].

1) Electrostatic Force: The electrostatic force is found from the changing capacitance as the GCA's fingers move and bend. Traditional models use a parallel plate approximation for capacitance, which results in deviations of up to 14% compared to FEM simulations at pull-in [12]. We derive a model for finger bending in the Appendix.

2) Damping: Between approximately rectangular plates, the squeeze-film damping coefficient is given by [13], with adjustments for the proximity of substrate below the fingers made in [14]. Accounting for both the front and back gaps:

$$b_{sf,f} = \left(\frac{\mu N S_1 S_2^3 \beta(\eta)}{(x_0 - x)^3}\right)\left(\frac{4(x_0 - x)^3 w_f + 2T_{ox}^3 T}{(x_0 - x)^3 w_f + 2T_{ox}^3 T}\right) \tag{3}$$

$$b_{sf,b} = \left(\frac{\mu N S_1 S_2^3 \beta(\eta)}{(x_b + x)^3}\right)\left(\frac{4(x_b + x)^3 w_f + 2T_{ox}^3 T}{(x_b + x)^3 w_f + 2T_{ox}^3 T}\right) \tag{4}$$

$$b = b_{sf,f} + b_{sf,b} \tag{5}$$

where μ_{air} is the medium's dynamic viscosity ($18.5\,\mu\text{Ns/m}^2$ for air and $888\,\mu\text{Ns/m}^2$ for water at STP), N is the number of fingers in the array, $S_1 = \max(L_{ol}, T)$, $S_2 = \min(L_{ol}, T)$, $\eta = \frac{S_2}{S_1}$ is the fingers' aspect ratio, $\beta(\eta) = 1 - 0.58\eta$ is a correction factor for the aspect ratio, and T_{ox} is the separation between the movable finger array and the substrate.

Previous work also includes shear-film Couette flow damping between the finger array and substrate [10]. Because of a GCA's small surface area, however, we find that squeeze-film damping is several orders of magnitude larger than shear-film damping along the fingers' trajectory, so we ignore the latter for this model. Shear-film damping would be more relevant for larger parts, such as the shuttle of an inchworm motor.

3) Spring Force: The movable fingers are supported by two parallel fixed-guided beams. The spring constant is determined from Euler beam theory to be

$$k = \frac{2E^* w_{spr}^3 T}{L_{spr}^3} \tag{6}$$

where E is the Young's Modulus of silicon (169 GPa), w_{spr} is the width of the beam, and L_{spr} is the length of the beam. $E^* = \frac{E}{1-\nu^2}$ is the effective Young's Modulus, as recommended by [15] since $w_{spr} \ll T$. However, since we fabricated our devices for this paper on a (100) silicon wafer with structural components along the [110] or [$\bar{1}$10] directions, $\nu = 0.069$ so $E^* = 170$ GPa $\approx E$ [16].

C. Release Dynamics Including Finger and Spine Deflection

Although the effect of voltage on GCA pull-in is well-documented [10], [11], since most dynamics analyses to date have focused on resonance instead of the discrete phases of traditional inchworm actuation [8], [9] the general intuition was that the drive voltage had little effect after it was released. In preliminary experiments, however, it was observed that the release time of GCA arrays noticeably changed based on the drive voltage during pull-in, but the cause was not well understood [10]. Here, we formulate a dynamics model that includes an initial velocity imparted from electrostatic finger bending and the compression of the central spine.

From the Appendix, at pull-in the fingers feel a distributed load from the electrostatic force. From Eq. 28, the stored potential energy of an N-finger array is NU_{es} before release.

The force from the GCA array also places axial strain on the spine, as shown in Fig. 3. This compresses the spine and stores potential energy, which is then imparted onto the array once the fingers are released. The spine's axial spring constant is given by

$$k_{spine} = \frac{EA_{spine}}{L_{spine}} \tag{7}$$

This article has been accepted for inclusion in a future issue of this journal. Content is final as presented, with the exception of pagination.

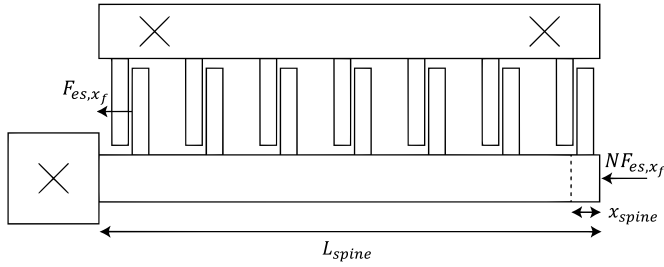RAUF *et al.*: NONLINEAR DYNAMICS OF LATERAL ELECTROSTATIC GCAs FOR APPLICATIONS IN INCHWORM MOTORS

3

Fig. 3. Model diagram for the axial deflection of the spine. The spine has a cross-sectional area A_{spine}. The dotted line represents the exaggerated axial deflection of the spine.

where A_{spine} is the cross-sectional area of the spine and L_{spine} is the length of the spine.

The axial deflection of the spine is given by N times the electrostatic force at the final position, divided by k_{spine}:

$$x_{spine} = \frac{N F_{es,x_f}}{k_{spine}} \quad (8)$$

The stored energy at the time of release will then be

$$U_{spine} = \frac{1}{2} k_{spine} x_{spine}^2 \quad (9)$$

The initial velocity of the entire array at release time can be found via energy conservation to be

$$v_{init} = \sqrt{\frac{2N U_{es} + 2U_{spine}}{m_{GCA}}} \quad (10)$$

We assume the fingers and spine transfer their stored energy to the full array very quickly (<1 μs), allowing us to ignore the losses or dynamics of this energy transfer. We also assume that the spine compression doesn't significantly affect the gaps between fingers at pull-in, i.e., that $x_{spine} \ll x_f$.

For a GCA with nominal dimensions as in Table I and pulled in at 60 V, the fingers contribute an estimated 105 pJ via our finger bending model and the spine contributes an estimated 49 pJ, highlighting how both factors are important to the release phase. If we had instead modelled F_{es} as a uniform load with the parallel plate approximation, the fingers would contribute only 62 pJ upon release, showing the significance of finger bending in release dynamics.

D. Gap Closer Dynamics in a Liquid

The dynamics of GCA arrays are similar in liquids but with significant modifications to the mass and damping terms. While the mass of air moved in a GCA array is negligible compared to the mass of the spine and fingers, the inertia of liquid moved during submerged actuation cannot be ignored. This additional mass can be found from continuity of flow.

From incompressible fluid mechanics,

$$A_c \dot{x}_c = A_w \dot{x}_w = A_f \dot{x}_f \quad (11)$$

where $A_c = 2(x_0 - x)(L_{ol} + T)$ is the effective area through which liquid is squeezed out of the closing gap, $\dot{x}_c$ is the average velocity of liquid squeezed out of that gap, $A_w = 2(x_b + x)(L_{ol} + T)$ is the effective area through which liquid enters the widening adjacent gap, $\dot{x}_w$ is the average velocity of liquid passing into that gap, $A_f = L_{ol} T$ is the finger overlap area, and $\dot{x}_f$ is the finger's velocity (we assume $\dot{x}_f \approx \dot{x}$).

Using substitution, the average velocity of liquid moving out of the closing gap and into the widening gap is, respectively,

$$\dot{x}_c = \frac{L_{ol} T \dot{x}_f}{2(x_c - x)(L_{ol} + T)} \quad (12)$$

$$\dot{x}_w = \frac{L_{ol} T \dot{x}_f}{2(x_w + x)(L_{ol} + T)} \quad (13)$$

The mass of liquid in these gaps is given by

$$m_c = \rho_l L_{ol} T (x_c - x) \quad (14)$$

$$m_w = \rho_l L_{ol} T (x_w + x) \quad (15)$$

where ρ_l is the density of the liquid. Considering the inertia associated with the mass and velocity of liquid in the closing and widening gaps for each finger, the inertial term of the dynamics model in Eq. 1 must be modified accordingly for actuation in liquid. This term is given by

$$m_{GCA,eff} \ddot{x} = \frac{d}{dt} \left(m_{GCA} \dot{x} + N \left(m_c \frac{\dot{x}_c}{2} + m_w \frac{\dot{x}_w}{2} \right) \right) \quad (16)$$

where the new effective mass is given by

$$m_{GCA,eff} = m_{GCA} + \frac{N \rho_l L_{ol}^2 T^2}{2(L_{ol} + T)} \quad (17)$$

III. MODELING

A. Model Setup

A dynamics model was developed in Python. The model takes the equations and initial conditions in the previous section and uses an ordinary differential equation (ODE) solver (RK45) to solve the displacement over time for the GCA array. Defining a state vector $X = [x, \dot{x}]^T$, the system dynamics for Eq. 1 are simulated for the initial conditions $X(t_{pull-in} = 0) = [0, 0]^T$ for pull-in, and $X(t_{release} = 0) = [x_0 - x_f, -v_{init}]^T$ for the release phase ($F_{es} = 0$). The simulation is terminated for pull-in time when $x = x_0 - x_f$ and for release time when $x = 0$. All code can be found at https://github.com/ahadrauf/gca_dynamics.

B. Pull-In and Release Times

We first run a parameter sweep over our simulation model to understand how the different GCA dimensions influence the pull-in and release times. Results are shown in Fig. 4. Finger length, finger width, initial front gap, and support spring width are varied for a GCA with nominal dimensions as in Table I.

The biggest influence on pull-in time is x_0, with a 25% decrease yielding a 30% decrease in pull-in time. Interestingly, L_{ol} is predicted to make minimal contribution to pull-in time near the nominal value due to its linear effect on both electrostatic force and damping, although it makes an larger impact for $L_{ol} < T$ due to the damping equation's $\beta(\eta)$ nonlinearity. In order, the biggest influences on release time are w_{spr}, with a 25% increase yielding a 47% decrease in release time; x_0, with a 25% increase yielding a 46% decrease in release time; L_{ol}, with a 25% decrease yielding a 22% decrease in release time; and w_f, with a 25% decrease yielding a 22% decrease in release time. Notably, release time is expected to increase as x_0 decreases, highlighting the importance of the support springs' force relative to damping. This analysis presents several options for optimizing motor performance.

This article has been accepted for inclusion in a future issue of this journal. Content is final as presented, with the exception of pagination.
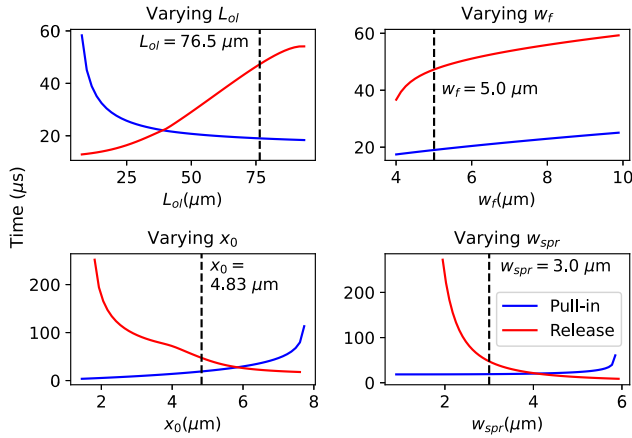
4

JOURNAL OF MICROELECTROMECHANICAL SYSTEMS

Fig. 4. Pull-in and release times are simulated while varying the finger overlap length, finger width, initial front gap, and support spring width. Nominal dimensions are listed in Table I, undercut is assumed to be $0.4\,\mu m$, and the drive voltage is 60 V. We also assume all experiments are conducted at STP.

TABLE I
NOMINAL DIMENSIONS (AS DRAWN IN LAYOUT) OF THE GCA ARRAYS USED IN THESE EXPERIMENTS

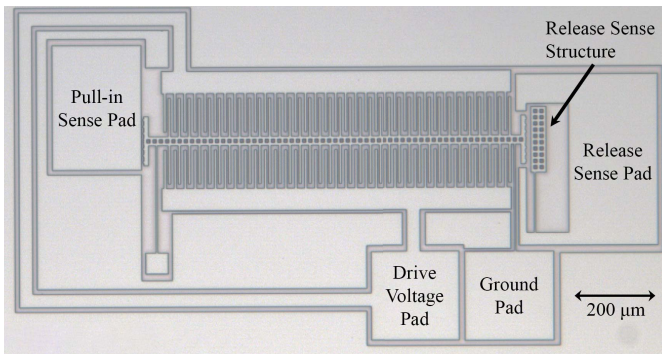| N	L_{ol}	x_0	x_f	x_b	w_f	w_{spr}
70	$76.5\,\mu m$	$4.83\,\mu m$	$1.0\,\mu m$	$7.75\,\mu m$	$5.0\,\mu m$	$3.0\,\mu m$

Fig. 5. The GCA test structure layout.

IV. METHODS

A. Detecting Gap Closure in Air

Fig. 5 shows the fabricated test structure. All devices are fabricated in a silicon-on-insulator (SOI) process as described in [10]. These SOI wafers have a $40\,\mu m$ device layer, $2\,\mu m$ buried oxide, and $550\,\mu m$ substrate. The experimental array varies the fingers' overlap length and the support springs' width, with nominal dimensions in Table I. The sense pads are tied to a 4V source through a pull-up resistor of order 1 MΩ. When the grounded spine makes contact with these pads, the sense signal drops, signaling the time of gap closure. The release sense structure is manually pushed left and held at $x = 0$ via a probe tip during experiments.

Fig. 6 shows a sample of the pull-in signals used for detection. The pull-in time is measured from the start of the pull-in voltage on the actuation signal (measured at 10% above the minimum) to the beginning of the signal drop on the sense signal (measured at 10% below the maximum). The sense signal slightly rises together with the actuation signal, attributed to either capacitive coupling or conductance through the substrate. Switch bounce was also noticeable upon contact.
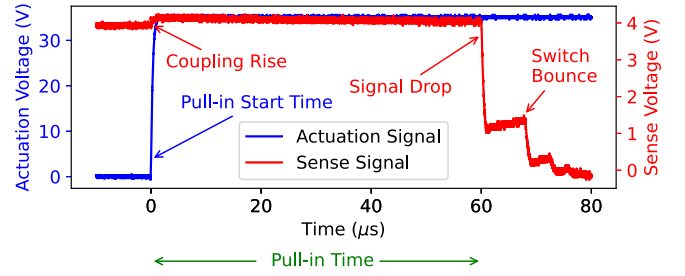

Fig. 6. A sample scope trace of the signals used to measure the pull-in time.
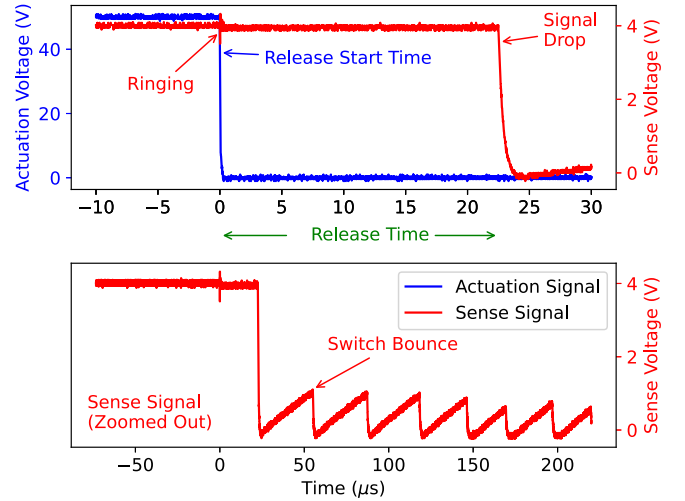

Fig. 7. A sample scope trace of the signals used to measure the release time, and a zoomed out image of the same sense signal trace showing obvious switch bounce.

Similarly, Fig. 7 shows a sample of the release signals. The release time is measured from the start of the release voltage on the actuation signal to the beginning of the signal drop on the sense signal. On the release signal trace, ringing is noticeable at the time of actuation signal drop, attributed to coupling in the measurement phase. Switch bounce is also present, shown in the zoomed out figure. The time interval between the first few bounces match our simulation results for an elastic collision between the sense pad and spine. However, the real system's half-period seems to decrease as its amplitude decreases for pull-in and release, likely because of unmodeled contact forces like the Van der Waals force or the air spring effect in the nonlinear squeeze-film damping equation [13].

B. Detecting Gap Closure in Water

A similar test structure was also fabricated to measure performance in deionized water. The main challenges of electrostatic MEMS operation in liquid are surface tension, electrolysis, and electrical conductivity [17]. Surface tension can create trapped gas bubbles and cause stiction if devices are dried, and is best addressed by submerging devices slowly to prevent bubble trapping and storing them in sealed containers to minimize evaporation losses. Electrolysis also creates gas bubbles and may lead to other chemical reactions that alter the electrodes or liquid medium, but can be prevented using a high-frequency AC drive signal instead of a DC drive signal [18]. Finally, liquids with high electrical conductivity will dissipate power, reducing the electrostatic actuator's efficiency.
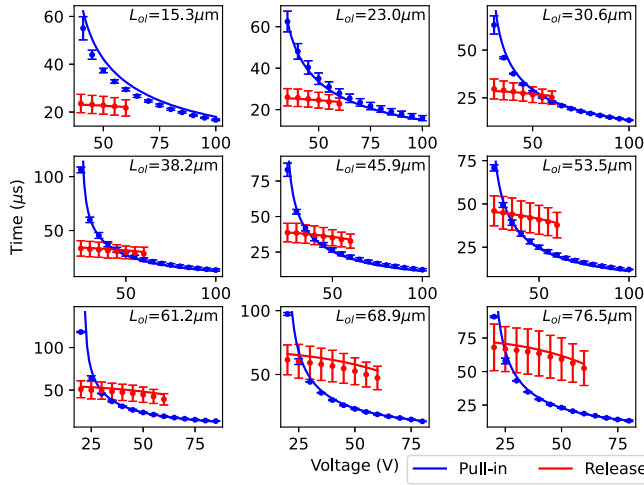
Fig. 8. Pull-in and release time measured and modelled while varying voltage for different overlap lengths in air.

Fig. 9. Pull-in and release time measured and modelled while varying voltage for different spring constants in air.

In this work, we highlight results measured in deionized water to avoid this issue, but we have also previously shown successful operation of gap closing actuators in a 10mM sodium dodecyl sulfate (SDS) solution [11]. For fabrication, Cr/Ru was selected for the metal layer over Au/Pd because of its strong adhesion to silicon in submerged devices and its conductive oxide [19]. Each device was tested using a 1 MHz AC square wave with zero-to-peak amplitudes from 0V to 6V.

V. RESULTS

A. Measurements in Air

1) Pull-in Time: Fig. 8 and Fig. 9 show the measured and modelled pull-in time as a function of voltage for varying overlap lengths and for varying support spring widths, respectively. Each measurement was tested across 4 different devices. We see the data matches reasonably well to our model - averaging across all devices, for Fig. 8, RMSE = 4.76 μs and mean absolute percentage error (MAPE) = 5.6%; and for Fig. 9, RMSE = 5.18 μs and MAPE = 4.8%. The simulated undercut process parameter is fit to each device via least squares (combining pull-in and release data) from the range 0.2 μm−0.5 μm, and despite individual device variation the average fit of 0.38 μm (σ = 0.07 μm) matches well with the 0.4 μm seen in prior studies [4], [10].

2) Release Time: Fig. 8 and Fig. 9 also show the measured and modelled release times during the aforementioned parameter sweeps. The simulated undercut for release time is the same as the one for pull-in time for each device. We see the results also match our model fairly well - averaging across all devices, for Fig. 8, RMSE = 1.79 μs and MAPE = 3.4%; and for Fig. 9, RMSE = 6.27 μs and MAPE = 6.3%. Notably, the pull-in and release times also follow our trend predictions in Sec. III-B (although specific values in Fig. 4 vary somewhat from the simulations here due to the fitted undercut).

B. Measurements in Water

Fig. 10 shows the pull-in time underwater as a function of voltage for varying overlap length. Compared to operation in air, GCAs submerged in deionized water have slower pull-in
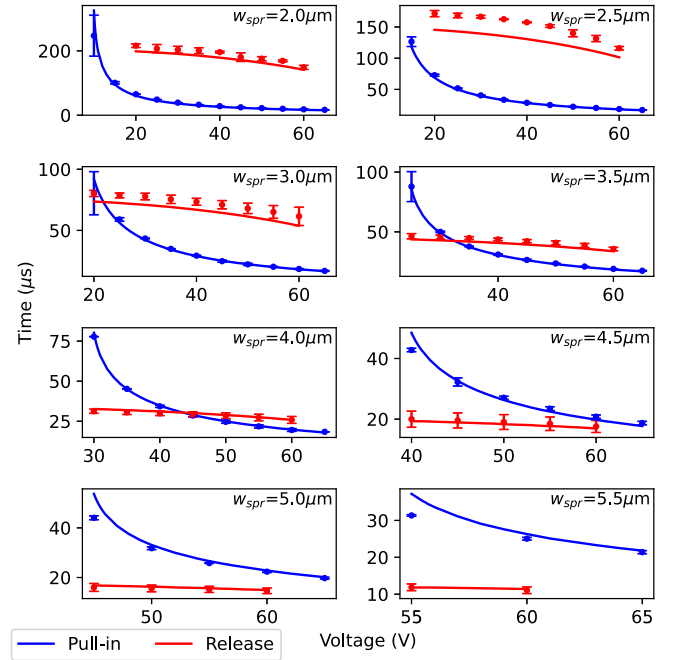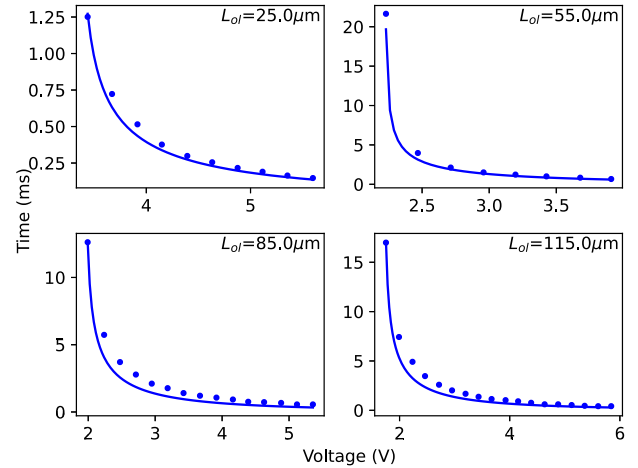

Fig. 10. Pull-in time measured and modelled while varying voltage for different overlap lengths in deionized water. The 55 μm device was damaged before testing up to 6 V.

times in exchange for higher force output, caused by water's relative permittivity of $\epsilon_r = 80$. Data was taken from [11] with authors' permission, although the simulation model is specific to this work. In simulation, our only change was to modify the medium's relative permittivity, density, and viscosity to water's standard values at STP. The results match our model well for small voltages and finger lengths but deviates a little otherwise, with RMSE = 0.559ms and MAPE = 20.6%. We predict this stems from our model underestimating water's damping force.

C. Inchworm Motor Speed

When integrating lateral GCAs into electrostatic inchworm motors, one practical application of decreasing pull-in and release times is increasing the max frequency with which the
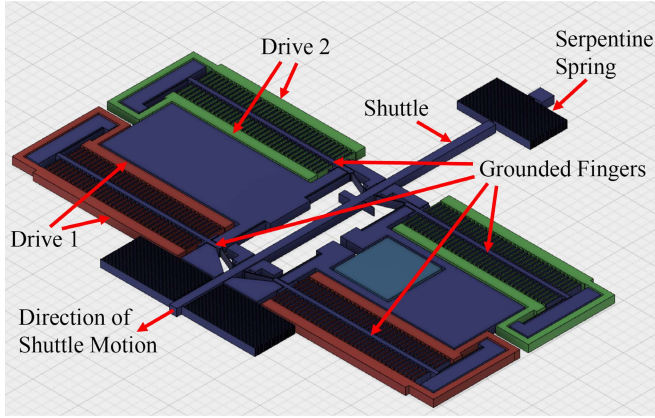
This article has been accepted for inclusion in a future issue of this journal. Content is final as presented, with the exception of pagination.

6

JOURNAL OF MICROELECTROMECHANICAL SYSTEMS

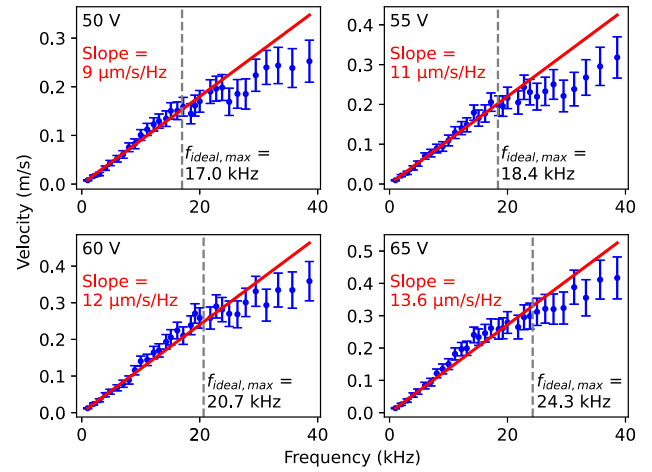Fig. 11.   The layout used for inchworm motor speed tests.

Fig. 12.   Velocity data measured for various voltages. The red line indicates the slope from the 4 lowest frequency data points. The vertical dotted line represents the maximum ideal frequency, described in Sec. V-C.

inchworm motor can still output its maximum force. We can apply the above GCA dynamics model to estimate this max frequency. We run our inchworm motors using the driving scheme in [2] with a 75% duty cycle; in other words, for a full period τ, the drive voltage is high for 0.75τ and low for 0.25τ. Fig. 3 in [2] provides a good pictorial depiction of the driving scheme. The structures are metallized with 60 nm sputtered TiN to lower the resistivity of sidewall contacts and to test the effect on motor longevity. Sidewall contact resistance was reduced from over 10 MΩ without TiN to 6-7 kΩ with TiN. The highest lifetime of a motor observed was 28 hours without TiN, and TiN did not noticeably improve device lifetime.

Denote t_P as the pull-in time when the GCA hits the gap stop, t_R as the release time when the GCA returns to zero position, t_{PT} as the time when the pawl first touches the shuttle during pull-in, and t_{RT} as the time when the pawl first releases the shuttle on release. Denoting the two actuators as A and B, there are four potential limits on the motor's maximum ideal frequency: we desire (1) having pawl A come in contact with the motor's shuttle before pawl B releases contact ($t_{PT} < t_{RT} + 0.25\tau$); (2) having pawl A fully pull-in before releasing its drive voltage ($t_P < 0.75\tau$); (3) having pawl B release the shuttle before its drive voltage is toggled again ($t_{RT} < 0.25\tau$); and (4) having pawl A fully settle before pawl B returns again ($t_P - t_{PT} < 0.5\tau$). We can define the maximum drive frequency for which we can expect full output force as $f_{ideal,max} = 1/t_{max}$, where t_{max} is the largest time constraint defined by (1)-(4). Given the accuracy of our simulations for t_P and t_R above, we choose to estimate t_{PT} and t_{RT} by shifting the endpoint of our simulation.

The testing structure (based on dimensions in Table I) is shown in Fig. 11 based on the similar layout in [10]. The pawl arm attached to each GCA at angle $\alpha = 65°$ makes contact with the inchworm motor shuttle at $x = x_f - 0.8\,\mu$m (factoring in an undercut of 0.2 μm for small feature sizes [12]). While the pawl is in contact with the shuttle, the GCA support spring constant in Eq. 6 is added to the pawl arm's spring constant, which is given via Euler beam theory to be

$$k_{pawl} = \frac{3E^*I_{pawl}}{L_{pawl}^3 \cos(\alpha)} \qquad (18)$$

The trace parasitics also affect the dynamics by adding an RC time constant when switching the drive voltage. Traces were not metallized in order to assess in the importance of RC effects on velocity. The device layer silicon we used has a resistivity of 10 Ω-cm, which means the high voltage traces should possess a resistance of 200 kΩ and the ground traces a resistance of 220 kΩ. The high voltage traces also have an estimated capacitance of 0.80 pF with the substrate.

We programmed our motor to take 10 steps at a specified frequency. Fig. 12 shows the resulting velocity, calculated by dividing the measured distance traveled by the time elapsed. As shown, inchworm motor performance begins to degrade from its linear improvement once $f > f_{ideal,max}$. Prior work at lower frequencies highlights expected velocity curves with slopes of 4 μm/s/Hz [10]. As we push our motors to higher speeds, however, the linear fits trend 2-3 times as much of a slope. Indeed, we achieved a maximum speed of 415 mm/s at 40 kHz, over 11$\times$ faster than the 35 mm/s reported previously at 8 kHz [10]. It was observed visually for low velocities that pawls will often push past the currently engaged pawls due to inertia, leading to larger step sizes. The parasitic RC factor only slightly reduced $f_{ideal,max}$ in simulation, highlighting that this driving scheme is relatively robust to parasitics.

Another influence from the parasitics is on power consumption. We can calculate the power consumption simply as

$$P = CV^2 f \qquad (19)$$

where f is the drive frequency. Prior experiments have measured the pull-in capacitance of a finger array with nominal dimensions to be 2.1 pF [12], so at 65 V we get an estimated power consumption of 9 nW/Hz for the actuator alone versus 12 nW/Hz with parasitics. This analysis continues the optimization discussion in Sec. III-B - shorter finger lengths, for example, have faster release times and thus can be driven faster with lower power consumption at the cost of lower output force. Alternatively, increasing the drive voltage improves t_P, t_R, and output force while increasing power consumption.

We also assume here that the shuttle is unloaded, although our analysis can easily be extended for a load force F_L on the shuttle by adding an offset $F_L \tan(\alpha)$ to the GCA's equation of

This article has been accepted for inclusion in a future issue of this journal. Content is final as presented, with the exception of pagination.

RAUF *et al.*: NONLINEAR DYNAMICS OF LATERAL ELECTROSTATIC GCAs FOR APPLICATIONS IN INCHWORM MOTORS   7

motion when simulating t_P, t_R, t_{PT}, and t_{RT}. A more rigorous analysis could add a coupled equation of motion for the shuttle with its own inertial and damping forces together with the pawl's contact friction and spring force (Eq. 18).

VI. CONCLUSION

In this work, we formalize a nonlinear dynamics model for laterally oriented electrostatic gap closing actuators. We systematically compare our model to experimental results over a variety of finger lengths and support spring constants in both air and deionized water mediums. We also highlight applications for these gap closing actuators in inchworm motors, showing that proper device optimization using these nonlinear models can allow for motors with large displacements, high force densities, and fast actuation.

APPENDIX
ELECTROSTATIC FORCE MODEL WITH FINGER BENDING

This derivation was inspired by [20], which applied the steps below to comb drive actuators where $x_0 = x_b$. We adapted the derivation to generalize to cases when $x_0 \neq x_b$. Although this derivation is quasistatic, we assume that it holds for our GCAs because our drive frequency is much less than the radial resonance frequency of an individual finger (1.0 MHz for a finger with nominal dimensions and $0.4\,\mu$m undercut [15]).

Denote x as the lateral deflection of the central spine, y as the lateral deflection of a single finger relative to the spine, and ζ as the position along the finger's length (with $\zeta = 0$ and $\zeta = 1$ indicating the finger's base and tip, respectively). Define the variables $g_0 = x_0 - x$ and $g_b = x_b + x$ as the effective front and back gaps for which our finger bending takes places. The transverse equilibrium of this finger is governed by

$$
E^* I \frac{d^4 y}{d\zeta^4}
$$
$$
= \begin{cases} 0 & \\ \quad 0 \leq \zeta \leq L - L_{ol} & \\ \frac{1}{2}\epsilon N L_{ol} T V^2 \left(\frac{1}{(g_0 - y)^2} - \frac{1}{(g_b + y)^2} \right) & \\ \quad L - L_{ol} \leq \zeta \leq L & \end{cases} \quad (20)
$$

where $E^* = \frac{E}{1-\nu^2}$ is the effective Young's modulus and $I = w_f^3 T / 12$ is the second moment of the beam. We ignore the effect of electrostatic fringing fields in this analysis for simplicity, instead addressing a simplistic model for it later. We also assume that only the spine's fingers bend to make Eq. 20 tractable, and we show later that this assumption is indeed close to FEM simulation results given $y \ll g_0$.

We can rewrite this equation as

$$
\frac{d^4 \tilde{y}}{d\tilde{\zeta}^4} = \begin{cases} 0 & 0 \leq \tilde{\zeta} \leq \alpha \\ \tilde{V}^2 \left(\frac{1}{(1 - \tilde{y})^2} - \frac{1}{(\beta + \tilde{y})^2} \right) & \alpha \leq \tilde{\zeta} \leq 1 \end{cases} \quad (21)
$$

with the substitutions $\tilde{y} = \frac{y}{g_0}$, $\tilde{\zeta} = \frac{\zeta}{L}$, $\alpha = \frac{L - L_{ol}}{L}$, $\beta = \frac{g_b}{g_0}$, and $\tilde{V}^2 = \frac{6\epsilon L^4}{E^* w_f^3 g_0^3} V^2$.

The finger is clamped at its base and is assumed to be free of loads at its tip ($\tilde{\zeta} = 1$), so the boundary conditions are:

$$
\text{at } \tilde{\zeta} = 0: \ \tilde{y} = \tilde{y}' = 0 \quad (22)
$$
$$
\text{at } \tilde{\zeta} = 1: \ \tilde{y}'' = \tilde{y}''' = 0 \quad (23)
$$

For small $\tilde{y}$, we can take the first-order Taylor expansion of the right side of Eq. 21 to get the linearized finger kinematics:

$$
\frac{d^4 \tilde{y}}{d\tilde{\zeta}^4} \approx \begin{cases} 0 & 0 \leq \tilde{\zeta} \leq \alpha \\ a + b\tilde{y} & \alpha \leq \tilde{\zeta} \leq 1 \end{cases} \quad (24)
$$

where $a = \left(1 - \frac{1}{\beta^2}\right) \tilde{V}^2$ and $b = \left(2 + \frac{2}{\beta^3}\right) \tilde{V}^2$.

The $\tilde{y}^0$ term is where the math for a gap closing actuator deviates from the derivation for a comb drive in [20]. The solution for Eq. 24 is given by

$$
\tilde{y}_1(\tilde{\zeta}) = b_0 + b_1\tilde{\zeta} + b_2\tilde{\zeta}^2 + b_3\tilde{\zeta}^3, 0 \leq \tilde{\zeta} \leq \alpha
$$
$$
\tilde{y}_2(\tilde{\zeta}) = -\frac{a}{b} + c_0 e^{-\lambda\tilde{\zeta}} + c_1 e^{\lambda\tilde{\zeta}} + c_2 \sin(\lambda\tilde{\zeta}) + c_3 \cos(\lambda\tilde{\zeta}),
$$
$$
\alpha \leq \tilde{\zeta} \leq 1 \quad (25)
$$

where $\lambda = b^{1/4}$, and $b_{0:3}$ and $c_{0:3}$ are constant parameters.

From the boundary conditions in Eq. 22, we can see that $b_0 = b_1 = 0$. For a continuous curve, we need the deflection $\tilde{y}$ and its three derivatives to be continuous at $\tilde{\zeta} = \alpha$:

$$
\tilde{y}_1(\alpha) = \tilde{y}_2(\alpha)
$$
$$
\tilde{y}_1'(\alpha) = \tilde{y}_2'(\alpha)
$$
$$
\tilde{y}_1''(\alpha) = \tilde{y}_2''(\alpha)
$$
$$
\tilde{y}_1'''(\alpha) = \tilde{y}_2'''(\alpha) \quad (26)
$$

The boundary conditions in Eqs. 26 and 23 can be written in the following matrix (27), as shown at the top of the next page.

We can obtain the electrostatic force by solving this matrix equation for the finger curvature parameters and then integrating the moment equation (20) over $L - L_{ol} \leq \zeta \leq L$.

We can also find the energy U_{es} stored in the bent finger by integrating the potential energy along $0 \leq \zeta \leq L$ using:

$$
U_{es} = \int_0^L \frac{1}{2} E^* I \kappa^2 d\zeta = \int_0^L \frac{1}{2} E^* I \left(\frac{(y'')^2}{[1 + (y')^2]^3} \right) d\zeta \quad (28)
$$

where κ is the curvature of the equation $y(\zeta)$, obtained by substituting $y = g_f \tilde{y}$ and $\zeta = L\tilde{\zeta}$ in Eq. 25, and y' and y'' are the first and second derivatives, respectively, of $y(\zeta)$ with respect to ζ.

Note that this derivation doesn't include the effect of fringing fields. Since the kinematic equations become difficult to solve incorporating a standard heuristic into the above process, we computed the final electrostatic force by multiplying the result of solving Eq. 27 by the heuristic Eq. 29 below. This heuristic was originally described in [21].

$$
F_{es,adj} = 1 + \frac{x_0 - x}{\pi w} \left(1 + \frac{t}{\sqrt{th + t^2}} \right) \quad (29)
$$

In Fig. 13, we simulated a GCA finger with nominal dimensions (Table I) using CoventorWare and compared the above F_{es} calculation with both a traditional parallel plate approximation and a numerical solution to Eq. 20 with boundary conditions in Eq. 22-23. Although the parallel plate model

$$\begin{bmatrix} -\alpha^2 & -\alpha^3 & e^{-\lambda\alpha} & e^{\lambda\alpha} & \sin(\lambda\alpha) & \cos(\lambda\alpha) \\ -2\alpha & -3\alpha^2 & -\lambda e^{-\lambda\alpha} & \lambda e^{\lambda\alpha} & \lambda\cos(\lambda\alpha) & -\lambda\sin(\lambda\alpha) \\ -2 & -6\alpha & \lambda^2 e^{-\lambda\alpha} & \lambda^2 e^{\lambda\alpha} & -\lambda^2\sin(\lambda\alpha) & -\lambda^2\cos(\lambda\alpha) \\ 0 & -6 & -\lambda^3 e^{-\lambda\alpha} & \lambda^3 e^{\lambda\alpha} & -\lambda^3\cos(\lambda\alpha) & \lambda^3\sin(\lambda\alpha) \\ 0 & 0 & \lambda^2 e^{-\lambda} & \lambda^2 e^{\lambda} & -\lambda^2\sin(\lambda) & -\lambda^2\cos(\lambda) \\ 0 & 0 & -\lambda^3 e^{-\lambda} & \lambda^3 e^{\lambda} & -\lambda^3\cos(\lambda) & \lambda^3\sin(\lambda) \end{bmatrix} \times \begin{bmatrix} b_2 \\ b_3 \\ c_0 \\ c_1 \\ c_2 \\ c_3 \end{bmatrix} = \begin{bmatrix} a/b \\ 0 \\ 0 \\ 0 \\ 0 \\ 0 \end{bmatrix} \tag{27}$$
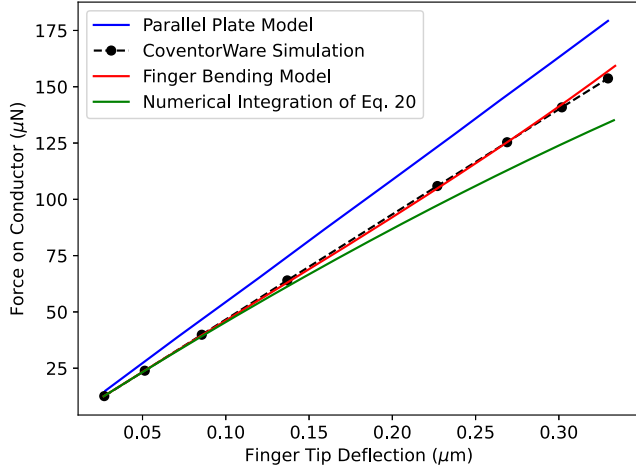

Fig. 13. CoventorWare was used to simulate the deflection at pull-in of the finger tip vs. electrostatic force on the finger with nominal dimensions (Table I) and drive voltages from 20–90 V. The finger bending model and fringing field multiplier match the FEM data with $r^2 = 0.9995$.

implies a 14% higher spring constant than simulation, a gap often called "spring softening" in literature for its effect on the resonance modes [8], the finger bending model and fringing field heuristic accurately model the real finger stiffness. Interestingly, our linearized kinematics match the FEM better than the numerical solution even at high voltages, perhaps due to nonlinearity in the fringing field for large deflections.

ACKNOWLEDGMENT

REFERENCES

[1] R. Yeh, S. Hollar, and K. S. J. Pister, "Single mask, large force, and large displacement electrostatic linear inchworm motors," *J. Microelectromech. Syst.*, vol. 11, no. 4, pp. 330–336, Aug. 2002.

[2] I. Penskiy and S. Bergbreiter, "Optimized electrostatic inchworm motors using a flexible driving arm," *J. Micromech. Microeng.*, vol. 23, no. 1, Jan. 2013, Art. no. 015018.

[3] C. B. Schindler, J. T. Greenspun, H. C. Gomez, and K. S. J. Pister, "A jumping silicon microrobot with electrostatic inchworm motors and energy storing substrate springs," in *Proc. 20th Int. Conf. Solid-State Sensors, Actuat. Microsyst. Eurosensors (TRANSDUCERS EUROSENSORS)*, Jun. 2019, pp. 88–91.

[4] D. Teal, H. C. Gomez, C. B. Schindler, and K. S. J. Pister, "Robust electrostatic inchworm motors for macroscopic manipulation and movement," in *Proc. 21st Int. Conf. Solid-State Sens., Actuators Microsyst. (Transducers)*, Jun. 2021, pp. 635–638.

[5] D. S. Contreras and K. S. Pister, "A six-legged MEMS silicon robot using multichip assembly," in *Proc. Hilton Head Solid-State Sens., Actuators Microsyst. Workshop*, 2018, pp. 1–5.

[6] J. I. Seeger and B. E. Boser, "Dynamics and control of parallel-plate actuators beyond the electrostatic instability," in *Proc. Transducers*, 1999, pp. 474–477.

[7] T. Singh *et al.*, "Modeling of low-damping laterally actuated electrostatic MEMS," *Mechatronics*, vol. 52, pp. 1–6, Jun. 2018.

[8] A. M. Elshurafa, K. Khirallah, H. H. Tawfik, A. Emira, A. K. S. A. Aziz, and S. M. Sedky, "Nonlinear dynamics of spring softening and hardening in folded-MEMS comb drive resonators," *J. Microelectromech. Syst.*, vol. 20, no. 4, pp. 943–958, Aug. 2011.

[9] S. P. Burugupally and W. R. Perera, "Dynamics of a parallel-plate electrostatic actuator in viscous dielectric media," *Sens. Actuators A, Phys.*, vol. 295, pp. 366–373, Aug. 2019.

[10] D. S. Contreras and K. S. J. Pister, "Dynamics of electrostatic inchworm motors for silicon microrobots," in *Proc. Int. Conf. Manipulation, Automat. Robot. Small Scales (MARSS)*, Montreal, QC, Canada, Jul. 2017, pp. 1–6.

[11] R. M. Shih, D. S. Contreras, T. L. Massey, J. T. Greenspun, and K. S. J. Pister, "Characterization of electrostatic gap-closing actuator arrays in aqueous conditions," in *Proc. IEEE Micro Electro Mech. Syst. (MEMS)*, Belfast, Ireland, Jan. 2018, pp. 596–599.

[12] D. Contreras, "Walking silicon: Actuators and legs for small-scale terrestrial robots," Ph.D. dissertation, Dept. EECS, Univ. California, Berkeley, Berkeley, CA, USA, May 2019.

[13] M. Bao and H. Yang, "Squeeze film air damping in MEMS," *Sens. Actuators A, Phys.*, vol. 136, no. 1, pp. 3–27, May 2007.

[14] M. Li, V. T. Rouf, and D. A. Horsley, "Substrate effect in squeeze film damping of lateral oscillating microstructures," in *Proc. IEEE 26th Int. Conf. Micro Electro Mech. Syst. (MEMS)*, Jan. 2013, pp. 393–396.

[15] R. J. Roark, W. C. Young, and R. G. Budynas, *Roark's Formulas for Stress and Strain*, 7th ed. New York, NY, USA: McGraw-Hill, 2002.

[16] M. A. Hopcroft, W. D. Nix, and T. W. Kenny, "What is the Young's modulus of silicon?" *J. Microelectromech. Syst.*, vol. 19, no. 2, pp. 229–238, Apr. 2010.

[17] D. Sameoto, T. Hubbard, and M. Kujath, "Operation of electrothermal and electrostatic MUMPs microactuators underwater," *J. Micromech. Microeng.*, vol. 14, no. 10, pp. 1359–1366, Oct. 2004.

[18] T. L. Sounart, T. A. Michalske, and K. R. Zavadil, "Frequency-dependent electrostatic actuation in microfluidic MEMS," *J. Microelectromech. Syst.*, vol. 14, no. 1, pp. 125–133, Feb. 2005.

[19] H. Over, "Surface chemistry of ruthenium dioxide in heterogeneous catalysis and electrocatalysis: From fundamental to applied research," *Chem. Rev.*, vol. 112, no. 6, pp. 3356–3426, Jun. 2012.

[20] D. Elata and V. Leus, "How slender can comb-drive fingers be?" *J. Micromech. Microeng.*, vol. 15, no. 5, pp. 1055–1059, 2005.

[21] V. Leus and D. Elata, "Fringing field effect in electrostatic actuators," Technion-Israel Inst. Technol., Haifa, Israel, Tech. Rep. ETR-2004-2, 2004.